Plasma Sources Science and Technology

PAPER • **OPEN ACCESS**

Experimental and computational investigations of electron dynamics in micro atmospheric pressure radio-frequency plasma jets operated in He/N_2 mixtures

To cite this article: L Bischoff *et al* 2018 *Plasma Sources Sci. Technol.* **27** 125009

OPEN ACCESS
IOP Publishing
Plasma Sources Science and Technology
Plasma Sources Sci. Technol. **27** (2018) 125009 (16pp)
https://doi.org/10.1088/1361-6595/aaf35d

Experimental and computational investigations of electron dynamics in micro atmospheric pressure radio-frequency plasma jets operated in He/N_2 mixtures

L Bischoff[1], G Hübner[1], I Korolov[1], Z Donkó[2], P Hartmann[2], T Gans[3], J Held[4], V Schulz-von der Gathen[4], Y Liu[5], T Mussenbrock[5] and J Schulze[1,6]

[1] Department of Electrical Engineering and Information Science, Ruhr-University Bochum, D-44780, Bochum, Germany
[2] Institute for Solid State Physics and Optics, Wigner Research Centre for Physics, Hungarian Academy of Sciences, H-1121 Budapest, Konkoly-Thege Miklós str. 29-33, Hungary
[3] York Plasma Institute, Department of Physics, University of York, Heslington,York, United Kingdom
[4] Experimental Physics II: Application Oriented Plasma Physics, Ruhr-University Bochum, D-44801 Bochum, Germany
[5] Electrodynamics and Physical Electronics Group, Brandenburg University of Technology Cottbus-Senftenberg, Cottbus D-03046, Germany
[6] Department of Physics, West Virginia University, Morgantown, WV 26506, United States of America

E-mail: schulze@aept.rub.de

Received 17 September 2018, revised 29 October 2018
Accepted for publication 23 November 2018
Published 28 December 2018

Abstract

The electron power absorption dynamics in radio frequency driven micro atmospheric pressure capacitive plasma jets are studied based on experimental phase resolved optical emission spectroscopy and the computational particle in cell simulations with Monte Carlo treatment of collisions. The jet is operated at 13.56 MHz in He with different admixture concentrations of N_2 and at several driving voltage amplitudes. We find the spatio-temporal dynamics of the light emission of the plasma at various wavelengths to be markedly different. This is understood by revealing the population dynamics of the upper levels of selected emission lines/bands based on comparisons between experimental and simulation results. The populations of these excited states are sensitive to different parts of the electron energy distribution function and to contributions from other excited states. Mode transitions of the electron power absorption dynamics from the Ω- to the Penning-mode are found to be induced by changing the N_2 admixture concentration and the driving voltage amplitude. Our numerical simulations reveal details of this mode transition and provide novel insights into the operation details of the Penning-mode. The characteristic excitation/emission maximum at the time of maximum sheath voltage at each electrode is found to be based on two mechanisms: (i) a direct channel, i.e. excitation/emission caused by electrons generated by Penning ionization inside the sheaths and (ii) an indirect channel, i.e. secondary electrons emitted from the electrode due to the impact of positive ions generated by Penning ionization at the electrodes.

Keywords: atmospheric pressure plasma jet, particle-in-cell simulation, electron heating, optical emission spectroscopy

1. Introduction

Radio-frequency (RF) driven microscopic atmospheric pressure plasma jets (μ-APPJs) are widely used as efficient sources of reactive species at low heavy particle temperatures for a broad variety of applications such as wound healing, sterilization, materials treatment/modification, and semiconductor manufacturing [1–8]. Typically, such jets are operated in helium with some admixtures of nitrogen and/or oxygen to produce reactive oxygen and nitrogen species. The generation of such reactive species is highly relevant for biomedical applications and for the removal of volatile organic compounds from exhaust gas streams [1, 2, 9, 10]. Reactive radicals are mainly generated by electron impact excitation/dissociation of the neutral gas. Therefore, the formation of the electron energy distribution function (EEDF) must be understood and controlled in order to optimize their generation. This, in turn, can be achieved by understanding and customizing the electron power absorption dynamics in these plasma sources. However, this is a challenging problem, since the EEDF is strongly space and time dependent within the RF period. Also, experimental and computational access to the EEDF is limited due to the small dimensions and short timescales of the experiment, as well as the computational effort required to simulate μ-APPJs due to the very high collisionality of these systems. Moreover, previous investigations [11, 12] have shown that, despite the high pressure and short mean free paths, kinetic effects play an important role. Therefore, kinetic approaches such as particle in cell simulations with Monte Carlo treatment of collisions (PIC/MCC) are required [13–17].

Previous investigations of the electron power absorption dynamics in μ-APPJs were mostly based on fluid models [18–21]. Experimentally, phase resolved optical emission spectroscopy (PROES, [22–25]) has often been used to study the dynamics of energetic electrons with high spatial and temporal resolution within the RF period. Often PROES measurements for different gas mixtures at atmospheric pressures are performed based on the *wavelength integrated* optical emission from the plasma (without using any optical filter) [23, 26–28]. In other cases, mainly when argon or oxygen is utilized, selected emission lines (e.g, Ar: 750 nm, O: 844 nm) are used [29–31]. The fact that different emission lines and the wavelength integrated (within the spectral response of a camera image sensor) radiation of the plasma are sensitive to different parts of the EEDF, is commonly disregarded in PROES measurements. Typically, this sensitivity is not known and/or is not taken into account in the analysis of such measurements. This strongly limits the comparability of different studies and the interpretation of the results. Wavelength integrated PROES measurements correspond to a complex, often unknown superposition of contributions of various emission lines with different sensitivities to specific energy regions of the EEDF. In order to clarify the sensitivity of a given emission line to different parts of the EEDF the population dynamics of the corresponding excited state must be clarified including electronic excitation from a variety of lower states, cascade contributions, excitation transfer, etc [32–37]. To understand, e.g. the generation of the plasma via ionization, an emission line must be chosen that is mostly sensitive to highly energetic electrons that are also responsible for the ionization. Only then the mode of discharge operation as the physical origin of the ionization in the plasma can be identified. The formation of reactive radicals via dissociation might be better understood by choosing an emission line that is sensitive to a lower electron energy domain.

RF driven μ-APPJs can be operated in two different electron power absorption modes, viz. the Ω- and the Penning-mode [23, 28, 38]. In the Ω-mode, maximum ionization occurs inside the plasma bulk at the time periods of sheath expansion and collapse at each electrode, when the current is maximum. Typically, local maxima of the ionization are observed on the bulk side of the expanding and collapsing sheath edges at both electrodes. In this mode, ionization is caused by energetic electrons accelerated by a high drift electric field inside the bulk at the times of maximum current within the RF period. The origin of this is the high collisionality of the discharge at atmospheric pressure, which leads to a low conductivity in the bulk and to a high electric field to drive the current through the bulk. Often, this mode is called α-mode [39–41]. However, this terminology is misleading, since it originates from low pressure capacitively coupled plasmas (CCPs), where sheath expansion heating [42] dominates and leads to the generation of energetic beam electrons during sheath expansion [43, 44], which propagate into the plasma bulk. Depending on the discharge conditions electric field reversals can cause ionization during sheath collapse in low pressure CCPs [45, 46]. While the spatio-temporal emission/excitation patterns observed in μ-APPJs operated in the Ω-mode look similar to those observed in low pressure CCPs operated in the α-mode, the underlying physical processes are significantly different in both types of discharges and, thus, different terminologies should be used to describe these two different electron power absorption modes.

A similar caveat exists with regard to the Penning mode in μ-APPJs [29, 47] and the γ-mode of low pressure CCPs [48, 49]. While ionization maxima are observed at the instantaneous sheath edge at the times of maximum sheath voltage within one RF period in both modes, their physical origins are markedly different and the same terminology should not be used to avoid misunderstandings. In the γ-mode of low pressure CCPs, the ionization maximum is caused by secondary electrons generated at the electrodes (typically by ion impact), which are accelerated towards the plasma bulk by

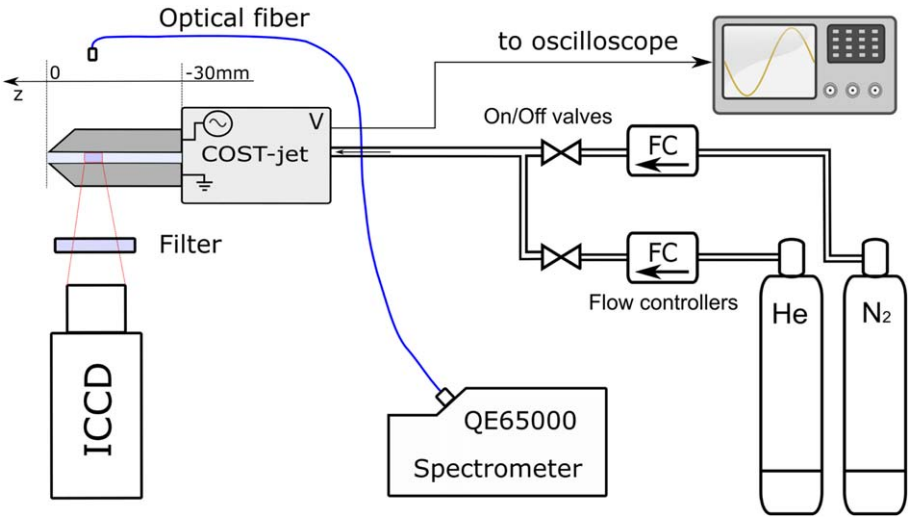

Figure 1. Schematic of the experimental set-up for phase resolved optical emission spectroscopy to investigate the electron dynamics in the COST-jet [39].

the sheath electric field and are multiplied by collisions inside the sheaths. In contrast to this, the Penning-mode of μ-APPJs operated in He/N_2 is based on Penning ionization, i.e. $He^* + N_2 \rightarrow He + N_2^+ + e^-$. If Penning ionization occurs within the sheaths, the resulting electron will be accelerated towards the plasma bulk by the sheath electric field and will be multiplied collisionally. However, the multiplication of these electrons is limited, since they are generated close to the maximum sheath edge (i.e. they do not propagate through the entire sheath). This happens due to the fact that the helium metastable density exhibits maxima at some distance from each electrode inside the sheaths [18]. The ions resulting from the Penning reactions will be accelerated towards the electrode, where they can cause emission of secondary electrons. These electrons will be accelerated towards the bulk by the sheath electric field and can be multiplied collisionally inside the sheath. Both pathways contribute to the characteristic excitation/emission maximum at the time of maximum sheath voltage within the RF period at both electrodes.

Generally, the details of the electron power absorption dynamics in RF driven μ-APPJs and mode transitions induced by changes of external control parameters such as the gas mixture and the driving voltage amplitude are not fully understood. Therefore, detailed insights are required for a knowledge based optimization of reactive species generation in these plasma sources.

Therefore, in this work we study the electron power absorption dynamics in RF driven μ-APPJs operated at 13.56 MHz in He/N_2 mixtures systematically by PROES. The experimental results are compared to those obtained from PIC/MCC simulations performed under identical conditions. Based on this comparison between experimental and computational results we improve the understanding of the electron dynamics in these discharges in three different ways: (i) we demonstrate that different spatio-temporal characteristics of the electron dynamics are obtained for different emission lines/bands and wavelength integrated PROES measurements. These differences are understood by revealing the population channels of the respective upper excited states for selected emission lines/bands and based on the simulation results. (ii) Mode transitions are observed and understood as a function of the N_2 admixture concentrations and the driving voltage amplitude in the experiment and in the simulation. (iii) We demonstrate that the Penning mode is based on two mechanisms: (a) a direct channel, i.e. excitation/ionization by electrons generated by Penning ionization inside the sheaths and (b) an indirect channel, i.e. secondary electrons emitted from the electrode due to the impact of positive ions generated by Penning ionization at the electrodes. This is revealed and quantified by switching secondary electron emission (SEE) from the electrodes on and off in the simulation and observing effects on the ionization maximum. The simulation results reveal that both channels contribute to the ionization to similar extents under the conditions studied in this work. It is also found that electron reflection from the electrodes plays a key role in the Penning mode.

The manuscript is structured in the following way: In the following section, the experimental setup and the simulation approach are introduced. In section 3, the results are shown and discussed. This part is divided into three sections according to the three novel insights into the electron dynamics in μ-APPJs, i.e. the sensitivity of PROES results to different emission lines, electron power absorption mode transitions, and the physical origins of the Penning mode. Finally, conclusions are drawn in section 4.

2. Experimental set-up and PIC/MCC simulation

2.1. Experiment set-up

A schematic view of the experimental set-up is shown in figure 1. Experiments are performed using a RF driven μ-APPJ operated in He with different N_2 admixture concentrations. The jet consists of two stainless steel electrodes of approximately identical dimensions covered by two quartz plates confining the

Table 1. Optical filters used in the experiment.

Central λ (nm)	FWHM (nm)	Species	Emission line, band (nm)	Transition	Energy threshold (eV)
390	10	N_2^+	391	$N_2^+(B) \rightarrow N_2^+(X)$	18.7
650	40	N_2	630–670	$N_2(B) \rightarrow N_2(A)$	7.4
700	15	He	706.5	$(3s)\ ^3S_1 \rightarrow (2p)\ ^3P_0$	22.7

discharge volume to 1 mm × 1 mm × 30 mm. Nevertheless, there is a small geometric asymmetry caused by the fact that the grounded surface area is slightly larger than the powered one. The electrode gap and width are 1 mm. The nozzle of the jet and the active plasma volume is located at $z = 0$ mm and $z < 0$ mm, respectively. Such jets are used as a reference source and are called COST reference micro plasma jets. More detailed information about the plasma source can be found in [39]. To calibrate the internal voltage probe of the jet, we followed the procedure described in [39] by using a commercial high voltage probe (Tektronix P6015A) and an oscilloscope (Tektronix TDS 2012B).

We use 5.0 purity helium and nitrogen gases, the flow rates are set to 1 slm and 0.5–5 sccm, respectively. In this way the reactive gas admixture is varied. The source is driven at $f = 13.56$ MHz by a power generator (Coaxial Power Systems RFG 150-13) via a matching network. The RF power is set so that the amplitude of the driving voltage waveform at the electrodes varies from 270 to 355 V, which corresponds to the range of conditions, at which a stable discharge can be generated. For the measurements, PROES (i) without any wavelength selection and (ii) with different interference filters is used to observe the emission from specific lines/bands according to table 1. The contribution of other lines/bands, that emit at wavelengths within the filter's transmission range, was checked using a high resolution Echelle spectrometer (ESA 4000, spectral range 200–780 nm, resolution of $\leqslant$0.02 nm) and it was found to be less than 5% of the specific line/band intensity for all conditions mentioned above. The emission is recorded space and time resolved within the RF period by an ICCD camera (LaVision Picostar HR equipped with a Canon MP-E 65 mm $f/2.8$ macro lens) with a gate width set to 1 ns, synchronized with the driving voltage waveform. The recorded image resolution corresponds to 149 pixels within the gap (1 mm) and 512 pixels (3.4 mm) in the direction of the gas flow. The central position of the image is located at approximately $z = -10$ mm inside the active discharge region. Based on the lens parameters, the electrode width, etc, the estimated spatial resolution of the PROES measurements is approximately 50 μm. To monitor the impurity level, time integrated optical emission spectroscopy (OES) measurements are also conducted using a USB grating spectrometer (Ocean Optics QE65000, spectral range: 200–980 nm, spectral resolution of 0.8 nm).

2.2. PIC/MCC simulation

The simulations are based on a symmetric bounded plasma electrostatic PIC code including Monte Carlo treatment of collision processes (PIC/MCC) [50–52] that is one dimensional in space and three dimensional in velocity space (1d3v). In the code, electrons as well as three ionic species, i.e. He^+, He_2^+, and N_2^+, are traced.

Electrons collide with He atoms and N_2 molecules of the background gas. For the electron–He atom collisions we use the cross sections from [53] while for electron–N_2 collisions the cross section set is adopted from [54]. (We note that this latter set is largely based on the Siglo cross section set, which is now accessible at the LxCat website [55].) The electron impact excitation rates from the ionic ground state of N_2^+ and the ground state of N_2 into the $N_2^+(B)$-state are computed based on the cross sections taken from [56, 57]. The excitation rates from the He I ground state into He I $(3s)^3S_1$ state are calculated by using the cross section adopted from [58]. All electron—atom/molecule collisions are assumed to result in isotropic scattering. When electrons collide with He atoms, 50% of the excitation is assumed to result in the formation of singlet (2^1S) or triplet (2^3S) metastable states either by direct excitation to these levels or by cascade transitions from higher-lying states [59]. The formation of these states is part of a very important ionization pathway, viz. the Penning ionization process (see later). For the different ionic species we only consider elastic collisions with the major constituent of the background gas, i.e. He atoms (which is justified by the low concentration of N_2 in the buffer gas):

- for He^+ ions the elastic collisions include an isotropic channel and a backward scattering channel [60],
- for He_2^+ ions, which are created via the

$$He^+ + He + He \rightarrow He_2^+ + He \quad (1)$$

process the Langevin cross section of the $He_2^+ + He$ collisions is considered, and

- for N_2^+ ions, which are created either by direct electron impact ionization or via the

$$He^* + N_2 \rightarrow He(1^1S) + N_2^+ + e^-. \quad (2)$$

Penning reaction, the Langevin cross section of $N_2^+ + He$ collisions is adopted as well.

We neglect chemionization processes (e.g. $He^* + He^* \rightarrow He^+ + He + e^-$ and $He_2^* + He_2^* \rightarrow He_2^+ + 2He + e^-$) due to the much lower density of atomic and molecular He metastables as compared to that of neutral nitrogen molecules. At these conditions and due to their specific rate coefficients these processes play a minor role for the electron/ion production. The treatment of the processes (1) and (2) in the simulation proceeds as follows. The rates of these reactions (which are adopted from [61, 62]) are used to assign a random

lifetime—according to the Monte Carlo approach—to each of the metastable atoms and He^+ ions upon their 'birth'. These particles are then placed on a wait list and the given conversion reaction is executed at a later time according to the (random) lifetime of the given particle (for more details see [59]).

In the simulation code, different time steps are used for the various species. The most demanding constraint is posed on the time step of the electrons due to their extremely high collisionality. In Monte Carlo simulations it is conventional to allow a collision probability $P = 1 - \exp(-\nu\Delta t)$ that amounts a few percent in a simulation time step of Δt (ν is the collision frequency). Here we set this limit at 10%, which results in a time step of $\Delta t_e = 4.5 \times 10^{-14}$ s for the electrons. The corresponding constraints for the ions allow significantly longer time steps. Therefore, we use the sub-cycling procedure for these species, with time steps of $\Delta t_{He^+} = 10\ \Delta t_e$ and $\Delta t_{He_2^+} = \Delta t_{N_2^+} = 100\ \Delta t_e$. These time steps, as well as the spatial numerical grid (that consists of 200 planes) satisfy the relevant stability criteria of the PIC scheme.

The neutral gas temperature is kept constant throughout this work at $T_g = 300$ K. For most of our studies the electron reflection probability at the electrodes is set to $\alpha = 0.5$. Data for this coefficient are highly scattered in the literature. Under the specific operating conditions of the experimental system the mean energy of the electrons reaching the electrodes is a few eV. For such conditions the above assumption is a good approximation for a variety of electrode materials [38, 46, 63]. The coefficient of ion induced emission of secondary electrons from the electrodes is set as $\gamma_{He^+} = 0.3$, $\gamma_{He_2^+} = 0.2$, $\gamma_{N_2^+} = 0.1$. For He^+ and N_2^+ ions these values are estimations based on [64–66], for He_2^+ we apply the findings of [67] that their yield is ≈60% of the yield of atomic ions. These surface coefficients are varied only in section 3.3 to reveal the physical origin of the Penning mode.

3. Results

3.1. Wavelength sensitivity of PROES in μ-APPJs

Figure 2 shows spatio-temporal plots of the measured plasma emission at different wavelengths according to table 1 (columns) and for different N_2 flows (rows) at a constant He flow of 1 slm. In each plot, the vertical axis spatially resolves the electrode gap, while the horizontal axis temporally resolves one RF period. Due to an effective geometric asymmetry of the jet (not considered in the simulations), which is caused by the larger grounded surface area compared to the powered surface area, most plots show some spatial asymmetry, i.e. the emission intensity is stronger adjacent to the bottom (powered) electrode compared to the top (grounded) electrode. The first column shows experimental results obtained from wavelength integrated PROES measurements performed without using any optical filter. Although PROES measurements at μ-APPJs are often conducted in this way [23, 26–28], these plots correspond to an unknown superposition of different emission lines/bands with a variety of excitation threshold energies and population dynamics of the upper excited level. Any sophisticated conclusions on the electron power absorption mode and dynamics are, therefore, hardly possible. We verify this statement by the fact that the spatio-temporal plots of the plasma emission at three selected wavelengths and obtained under the same discharge conditions are markedly different (see columns 2–4 of figure 2). For all N_2 admixture concentrations, the wavelength integrated PROES measurements show two emission maxima per RF period at the times of sheath expansion at both electrodes with strong emission in the plasma bulk. These maxima occur at the times of maximum current and are caused by high drift electric fields in the plasma bulk due to a low conductivity because of the high electron-neutral collision frequency at atmospheric pressure.

The spatio-temporal plots obtained from PROES measurements performed with an optical filter with a central wavelength of 390 nm (second column of figure 2) are dominated by emission from the $N_2^+(B \rightarrow X)$ molecular band at 391 nm with an energy threshold for electron impact excitation from the ground state of N_2 into the $N_2^+(B)$-state of 18.7 eV (see table 1). For the highest reactive gas flows of 2.5 and 5 sccm, these results look qualitatively similar to the wavelength integrated PROES measurements. However, there is a significant difference at the lowest N_2 flow of 0.5 sccm, for which the N_2^+ band shows almost no emission in the plasma bulk, but only adjacent to the sheath edges.

In order to understand such details of these spatio-temporal plots, the population dynamics of the upper excited state of the observed transition at 391 nm, N_2^+ ($B\ ^2\Sigma_u^+$), must be understood. As illustrated by figure 3, it is mainly populated via three different pathways [35, 68]: (I) electron impact excitation from the ground state of N_2, (II) electron impact excitation from the ionic ground state of N_2^+ and (III) Penning ionization, i.e. $He^* + N_2 \rightarrow He + N_2^+(B) + e^-$. Via processes (I) and (III) the nitrogen molecule is ionized and the resulting ion can be excited simultaneously. Other states of N_2^+ including its ground state, $N_2^+(X)$, can be populated via channel (III) as well. De-excitation by spontaneous emission from the $N_2^+(B)$-state into the ground state of the N_2^+ ion results in the observed emission at 391 nm. The population of the $N_2^+(B)$-level by cascades and via ion-molecular reactions with He_2^+ ions can be neglected, since this level has a relatively high energy and according to the simulations the production rate of He^* is much higher than that of He_2^+ ions. Electron impact excitation from the ground state of N_2 and from the ionic ground state of $N_2^+(X)$ into the $N_2^+(B)$-state [pathways (I–II)] is space and time dependent within the RF period, since it is caused by energetic electrons accelerated by the space and time dependent electric field in the plasma. However, the population of the $N_2^+(B)$-state via Penning ionization [pathway (III)] can be considered as time independent, since it is induced by He metastables, whose density according to the simulations is approximately constant (in a range of 5%) in time within the RF period. Based on these arguments the spatio-temporal plots of the emission can be split into two parts corresponding to the excitation pathways (I–II) and (III) of the upper state (see figure 4). At each spatial

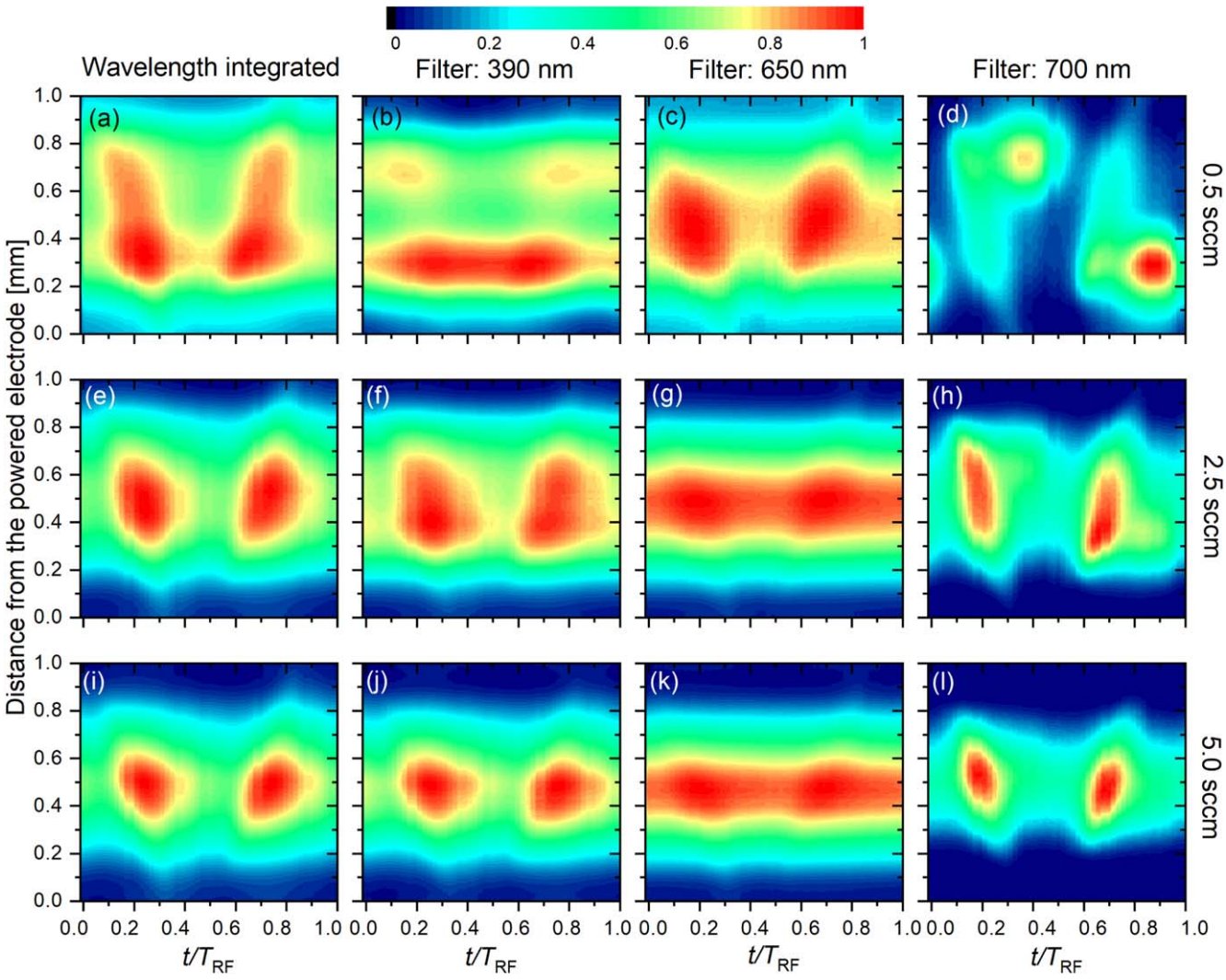

Figure 2. Normalized (to the maximum value of each data set) spatio-temporal emission plots obtained from wavelength integrated and wavelength selective PROES (columns) at various N_2 gas flows (rows). The powered electrode is located at $x = 0$, while the grounded electrode is located at $x = 1$ mm. The driving frequency, voltage amplitude, and the He flow are $f = 13.56$ MHz, $\phi = 315$ V, and 1 slm, respectively.

position, the contribution of pathway (III), i.e. Penning ionization, to the total emission is identified as the temporally constant 'background' emission, which corresponds to the minimum emission within the RF period. After its subtraction from the total emission, the remaining spatio-temporal data corresponds to the sum of the emission caused by electron impact excitation from the ground state of N_2 [pathway (I)] and from the ionic ground state of N_2^+ [pathway (II)]. The results of this analysis are shown in figure 4 for different admixture concentrations of N_2. The first row shows the total measured spatio-temporal emission at 391 nm. In the second row, the sum of the emission caused by electron impact excitation from the ground state of N_2 [pathway (I)] and from the ionic ground state of N_2^+ [pathway (II)] is shown after subtracting the temporally constant background at each spatial position from the data shown in the first row. The third row shows the total electron impact excitation rate obtained from the simulation and the individual contributions of the time modulated excitation [pathways (I) and (II), row 4] and of the temporally constant pathway (III) (row 5) obtained from the simulation, respectively. The sixth row shows the spatial profiles of the plasma emission caused by Penning ionization [pathway (III)] obtained from the simulation and the experiment.

The contribution of the Penning ionization/excitation to the plasma emission is almost constant in time. Experimentally, it corresponds to the minimum emission at each spatial position. The good agreement between the experimental and simulation results for all pathways verifies that our analysis of the population dynamics of the upper excited state of this band is justified. Due to the lower threshold energy for electron impact excitation from $N_2^+(X)$ into $N_2^+(B)$ compared to the energy threshold for electron impact excitation from the neutral ground state of N_2 into $N_2^+(B)$, the maxima shown in row 5 of figure 4 are significantly broader in time compared to the maxima shown in row 4. This is caused by the presence of an approximately harmonic modulation of the bulk electric field, which causes an acceleration of electrons above a low

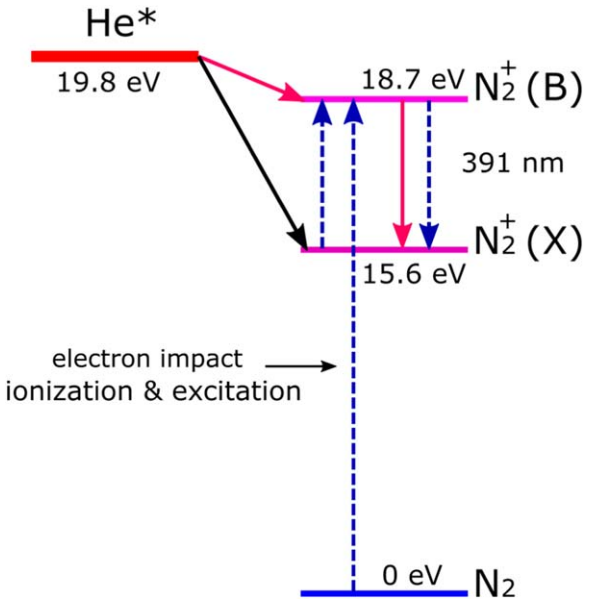

Figure 3. Simplified energy level diagram showing the dominant population pathways of the N_2^+ (B) level. The dashed blue lines indicate pathways that are space and time dependent within the RF period, since they are induced by energetic electrons accelerated by the space and time dependent RF electric field. The solid lines indicate pathways, which are induced by heavy particle interactions between He metastables and nitrogen molecules (Penning ionization) and are space, but not (negligibly small) time modulated within the RF period.

energy threshold for a larger fraction of the RF period compared to the acceleration of electrons above a high energy threshold. Figure 4 also shows that the electron impact excitation from the ionic ground state into the N_2^+(B)-state decreases as a function of the N_2 admixture. This is caused by the fact that a smaller fraction of the N_2 molecules is ionized at high, compared to low N_2 admixtures. Overall, this analysis yields an understanding of the observed spatio-temporal plasma emission at 391 nm.

Based on these fundamental insights, the differences between the wavelength integrated PROES measurements and those performed at 391 nm observed in figure 2 for 0.5 sccm N_2-flow can now be understood. These differences are caused by the fact that the electron impact excitation of the N_2^+(B)-state and, thus, the plasma emission at 391 nm are more sensitive to energetic electrons [via pathway (I)] than the wavelength integrated PROES measurements. Due to the decrease of the plasma density from the center towards the electrodes and the corresponding decrease of the conductivity and the increase of the drift electric field, energetic electrons are predominantly present adjacent to the sheath edges. Thus, at 391 nm and for low N_2 admixtures, emission is predominantly observed adjacent to the instantaneous sheath edges, while the wavelength averaged PROES measurements also show strong emission in the discharge center. Admixing more N_2 increases the collisionality and, thus, the drift electric field at the times of maximum current within the RF period. This results in the presence of more energetic electrons also in the discharge center and, therefore, to higher emission intensity of the nitrogen ion band in the plasma bulk.

PROES results obtained from a nitrogen molecular band around 650 nm, which is a part of the 1st positive $N_2(B) \rightarrow N_2(A)$ system with an excitation threshold of 7.4 eV, are shown in the third column of figure 2. These measurements show a much weaker dynamics compared to columns 1, 2, and 4 of this figure. This is caused by the sensitivity of this emission band to electrons with lower energy. There is an approximately sinusoidal oscillation of the bulk electric field with extrema at the times of maximum current within the RF period and zero-crossings at the times of vanishing current. This means that emission from lines/bands that are only sensitive to highly energetic electrons is only observed within narrow time intervals, when the drift field is high, whereas emission from lines/bands that are sensitive to lower energetic electrons is observed during much longer time intervals within a given RF period. The population dynamics of the upper states of this emission band is complicated, since it includes cascading transitions from different higher states [69] influencing its temporal structures. Therefore, this band can hardly be used to obtain any detailed understanding of the electron dynamics.

Finally, the fourth column of figure 2 shows spatio-temporal plots of the emission resulting from a He line with an energy threshold for electron impact excitation from the ground state of 22.7 eV (see table 1). The upper state can also be populated by electron impact excitation from the (1s2s) ^{3}S metastable state of helium. The cross section of this process [70] is approximately two orders of magnitude higher than the cross section for electron impact excitation from the ground state of He [71]. Nevertheless, at atmospheric pressures, the helium metastable density for all cases studied here is eight orders of magnitude less than the He ground state density (see also [18]). Taking into account the EEDF from the simulations, we have estimated that the upper state is populated predominantly (about 99%) by direct electron impact excitation from the ground state. Therefore, the spatio-temporal plots for this line are sensitive to highly energetic electrons and, thus, probe the ionization dynamics, identify the mode of electron power absorption and the way the plasma is sustained. Comparison to PIC/MCC simulation results is also straightforward as electron impact excitation from the ground state to the corresponding upper state is easily included based on the cross section given in [53]. The He line shows markedly different dynamics compared to the other cases displayed in figure 2. It generally exhibits a much stronger dynamics and, at the lowest N_2 admixture of 0.5 sccm, it shows ionization maxima at the sheath edges at the times of maximum sheath voltages within the RF period. Thus, this He emission line indicates that the discharge is predominantly operated in the Penning-mode, while the other lines/bands indicate operation in the Ω-mode. Any interpretation of the mode of discharge operation based on these other lines, however, could be misleading, since those do not trace the most energetic electrons, which generate the plasma by ionization. Only the behavior of this He line is connected with these electrons and shows that those result from Penning ionization for low N_2 admixtures. As the reactive gas flow is increased, a mode transition from the Penning- into the

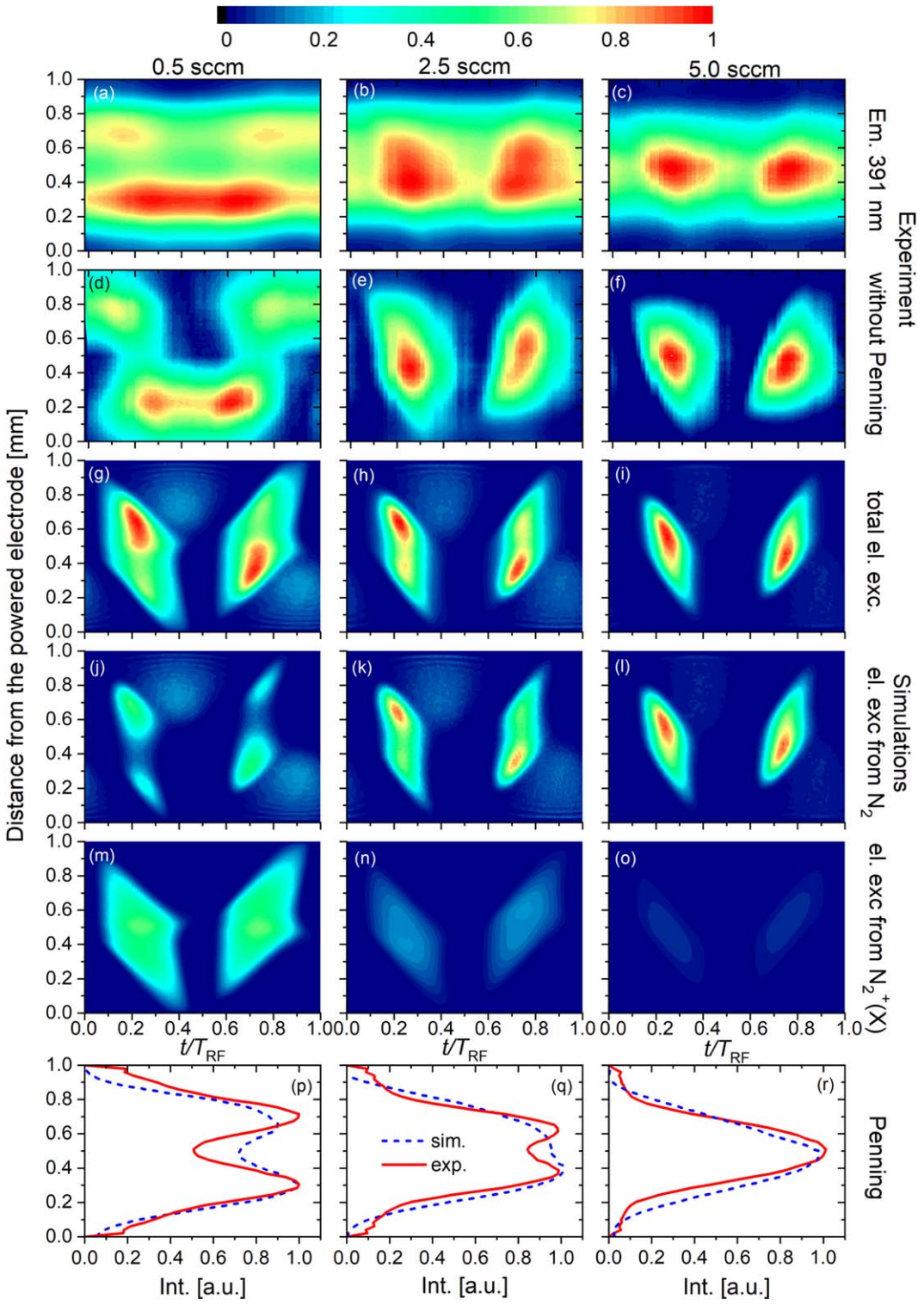

Figure 4. Spatio-temporal plots for different N_2 admixtures of the measured and individually normalized emission at 391 nm ((a)–(c)), of the time modulated component of the data shown in the first row ((d)–(f)), of simulation results of the total electron impact excitation rate into the N_2^+(B)-state (pathways (I) + (II), (g)–(i)), the electron impact excitation rate from the molecular ground state (pathway (I), (j)–(l)) and the ionic ground state (pathway (II), (m)–(o)) of N_2 into the N_2^+(B)-state. Plots (p)–(r) show the spatial profiles of the normalized time averaged excitation rate of the N_2^+(B)-state via Penning ionization obtained from the simulation (red lines) and of the temporally constant component of the total emission obtained from the experiment (blue dashed lines). Data are shown for $\phi = 315$ V.

Ω-mode is induced, since the collisionality of the discharge is increased and the energy gain of electrons generated as a result of Penning ionization inside the sheaths gets less efficient. As a result, there is no collisional avalanche of these electrons inside the sheaths and the characteristic ionization maximum gets weaker, i.e. the mode of discharge operation changes.

These results clearly show that great care must be taken, when selecting emission lines/bands for PROES measurements

in these plasmas, since misinterpretations are possible, if inappropriate choices are made.

3.2. Electron power absorption mode transitions

Based on the insights obtained in the previous sections, the He I emission line at 706.5 nm is chosen to study the mode of discharge operation of a RF driven μ-APPJ operated in He as a function of the N_2 admixture and the driving voltage amplitude. This line is chosen, since it traces highly energetic electrons above 22.7 eV, because its excited state is predominantly populated by electron impact excitation from the ground state at this threshold energy.

Figure 5 shows measured spatio-temporal plots of the plasma emission at 706.5 nm (first row) and simulation results for the electron impact excitation rate from the He I ground state into the He I $(3s)^3S_1$-state (second row) for different driving voltage amplitudes of 270, 315, and 355 V (columns) at constant flow rates of 1 slm of He and 2.5 sccm of N_2. In case of the experimental results the time axes are shifted so that the measured emission and the calculated excitation maxima occur at the same time so that they can be compared directly. Naturally, there is a short delay of a few nanoseconds between excitation and emission, which is neglected here. At atmospheric pressure this delay is particularly short due to the very efficient collisional de-excitation [72]. Our kinetic PIC/MCC simulations also provide space and time resolved access to the electron energy probability function (EEPF), that determines a variety of important processes such as excitation, dissociation, and ionization of the neutral gas. Based on the spatio-temporal plots of the electron impact excitation rate obtained from the simulation, we define regions of interest (ROI) around the dominant excitation maxima adjacent to the top electrode within one RF period, according to figures 5(d)–(f). These cover the 'Penning'-maximum inside the sheath at times of maximum sheath voltage and the 'Ω'-maximum on the bulk side of the local sheath edge during its expansion phase. By averaging over space and time within each ROI we determine the respective EEPF for this ROI. Moreover, we determine the 'averaged' EEPF by averaging over the entire electrode gap and one RF period. Based on this, further panels of figure 5 depict the computed EEPF in these ROIs as well as on space and time average (third row). Moreover, the computed time averaged spatial distributions of the helium metastable density (fourth row) are shown. In these simulations, the ion induced secondary electron emission coefficient (SEEC) is set to 0.1, 0.3, and 0.2 for N_2^+, He^+, and He_2^+ ions, respectively, and the electron reflection probability at the electrodes is 50%. We note that for all conditions studied here and according to the simulation results, N_2^+ ions are the dominant ionic species, while the densities of He_2^+ and He^+ ions are negligible. Thus, only the choice of the SEEC for N_2^+ ions affects the simulation results significantly. Excellent agreement between experimental and computational results is found for all voltages. Similar to α- to γ-mode transitions in low pressure CCPs [48, 73–75], a mode transition from the Ω- to the Penning-mode is induced by increasing the driving voltage amplitude. This is caused by the increase of the sheath electric field as a function of the driving voltage amplitude. Thus, at higher voltages electrons generated by Penning ionization and ion induced secondary electrons generated at the electrodes can gain more energy and more efficient electron avalanches build up at the times of maximum sheath voltage within each RF period. Therefore, the emission/excitation maxima at the times of maximum sheath voltage at the instantaneous sheath edge increase relative to the maxima caused by the drift electric field in the bulk at the times of sheath expansion/collapse.

Such mode transitions and their understanding are of outmost importance, since they strongly affect process relevant plasma parameters such as the plasma density, which is higher in the Penning - compared to the Ω-mode. Our simulation results show clear contributions of ionization by ion induced secondary electrons to the ionization maxima at the times of maximum sheath voltage within the RF period. Such secondary electrons cause the striated excitation patterns shown in figures 5, 6(d)–(f). After being generated at the electrodes they are accelerated towards the bulk by the sheath electric field and cause excitation repeatedly. Similar to the Franck–Hertz experiment, we observe striations in the excitation patterns near the electrodes due to non-equilibrium effects of the electron transport [76–82]. In the spatial and temporal domains where the striations appear, the reduced electric field is within the 'window' of its values where periodic relaxation of the electron velocity distribution function (VDF) is expected [83–85]. As an example, the reduced electric field for the case of 0.5 sccm nitrogen flow and 315 V voltage amplitude (figure 6(d)) at a time of $t/T_{RF} = 0.2$ and at a distance of 0.9 mm from the powered electrode is $E/N \approx 30$ Td. Thus, the appearance of striations in the simulation results is justified. It is, however, not completely clear why these structures are not seen experimentally. As the COST-jet operates in open air environment [86], we identify the presence of impurities (e.g. traces of water vapor) as the primary reason that can be responsible for changing the characteristics of the VDF near the electrodes. As these impurities have significantly lower excitation threshold energies as compared to He, extremely small amounts may lead to the disappearance of these structures, while the overall behavior of the plasma is not changed due to the small energy losses of the electrons while interacting with these impurities. Another reason why the striations are not observed experimentally might be the confinement of the plasma by the quartz plates, which, due to edge effects, might cause an apparent smoothing of the striations.

Turning now to the analysis of EEPFs, we generally observe significant spatial and temporal variations of this function with the discharge conditions (figures 5(g)–(i)). The EEPF within the sheath regions indicated as 'Penning' in these panels, extends gradually to higher energies as the excitation voltage amplitude is increased. This is a result of higher sheath electric fields at higher driving voltage amplitudes, which allow electrons within the sheaths to be accelerated to higher energies. The increased excitation rate at

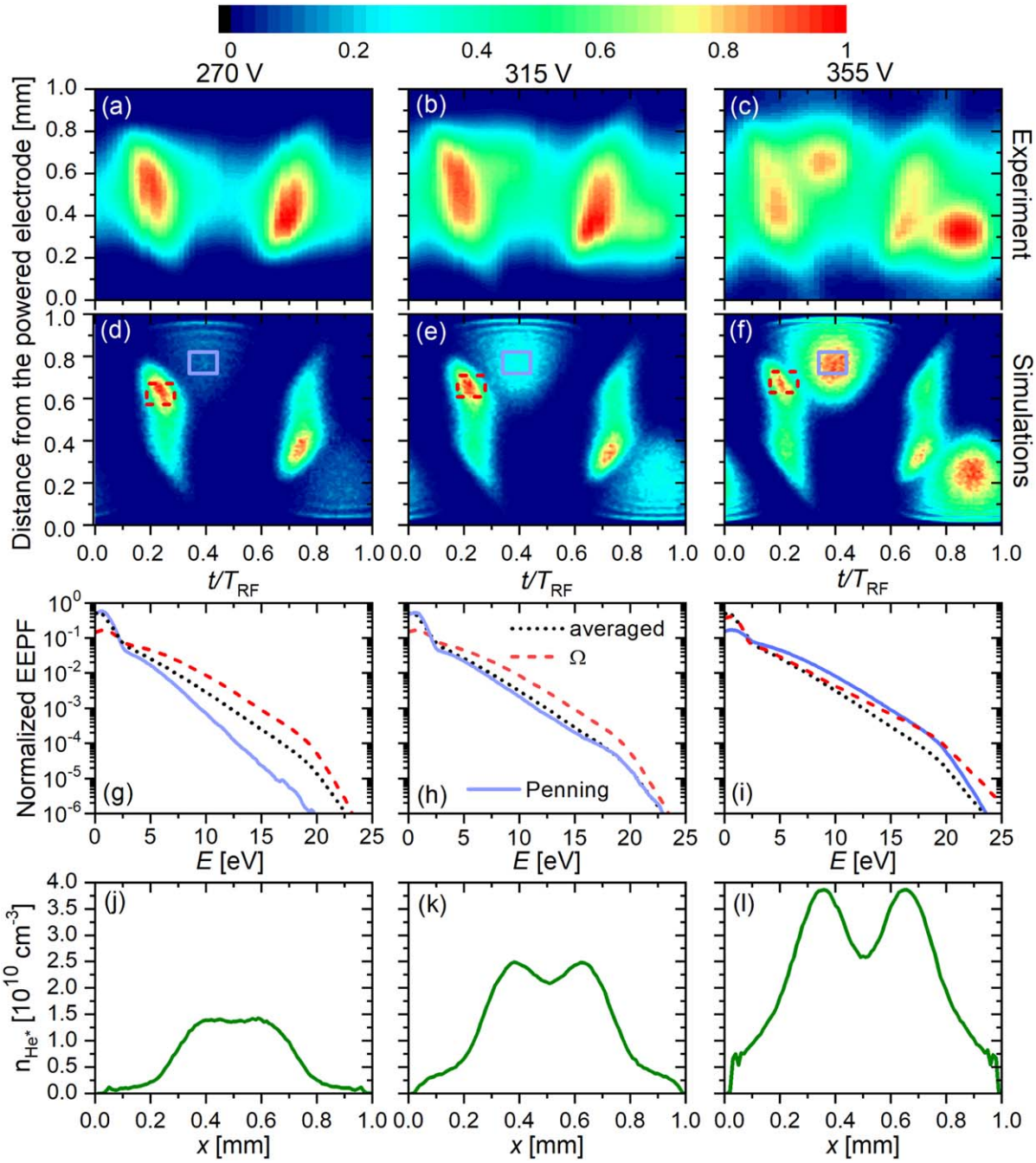

Figure 5. Measured normalized spatio-temporal plots of the emission of the 706.5 nm He I line (first row) and of the computed electron impact excitation rate from the He I ground state into the He I $(3s)^3S_1$-state (second row), computed EEPFs (third row), and computed time averaged spatial distributions of the helium metastable density (fourth row). EEPFs are shown for regions of interest indicated in panels (d)–(f) around the 'Penning'-maximum inside the sheath, the 'Ω'-maximum on the bulk side of the expanding sheath edge and 'averaged' over the electrode gap and one RF period. Results are shown for different driving voltage amplitudes (columns). The powered electrode is situated at $x = 0$, while the grounded electrode is located at $x = 1$ mm. Discharge conditions: 13.56 MHz, 1 slm He flow, 2.5 sccm N_2-flow. In the simulation the ion induced SEEC is set to 0.1, 0.3, and 0.2 for N_2^+, He^+, and He_2^+ ions, respectively, and the electron reflection probability at the electrodes is 50%.

higher voltages is the consequence of this change of the EEPF (see panels (d)–(f)). The change of the EEPF near the edge of the expanding sheaths, indicated as 'Ω' in panels (g)–(i) is less pronounced. The spatio-temporally averaged EEPF (marked as 'averaged') is rather insensitive to the discharge conditions. The density distributions of the metastable atoms (panels (j)–(l)) highly correlate with the behavior of the EEPFs and the spatio-temporal excitation dynamics. As these levels can only be populated by highly energetic electrons, an increasing high energy tail of the EEPF largely enhances the metastable density. The two-peaks structure of the latter observed at high driving voltage (seen in panels (k)–(l))

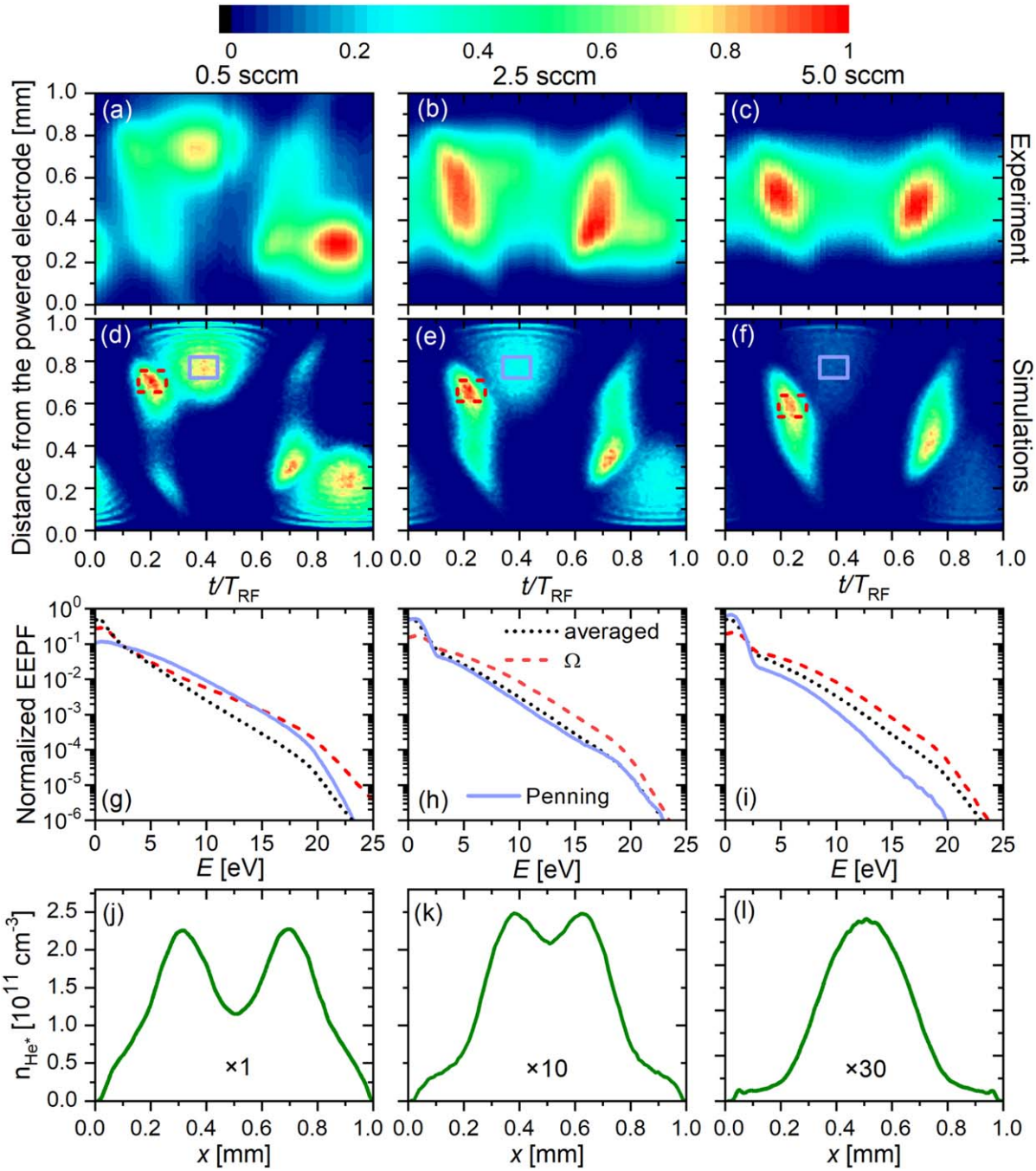

Figure 6. Measured normalized spatio-temporal plots of the emission of the 706.5 nm He I line (first row) and spatio-temporal plots of the electron impact excitation rate from the He I ground state into the He I $(3s)^3S_1$-state obtained from the simulations (second row), computed EEPFs (third row), and computed time averaged spatial distributions of the helium metastable density (fourth row). EEPFs are shown for regions of interest indicated in panels (d)–(f) around the 'Penning'-maximum inside the sheath, the 'Ω'-maximum on the bulk side of the expanding sheath edge and 'averaged' over the electrode gap and one RF period. Results are shown for different flows of N_2 at a constant He flow of 1 slm (columns). The powered electrode is situated at $x = 0$, while the grounded electrode is located at $x = 1$ mm. Discharge conditions: 13.56 MHz, 315 V. In the simulation the ion induced SEEC is set to 0.1, 0.3, and 0.2 for N_2^+, He^+, and He_2^+ ions, respectively, and the electron reflection probability at the electrodes is 50%.

emerges due to the efficient excitation within the sheaths caused by the strong Penning maximum. In contrast to this, at low driving voltage amplitudes the discharge is operated in the Ω-mode and maximum excitation occurs closer to the discharge center and, thus, the helium metastable density shows a broad maximum in the center as well.

Figure 6 shows measured spatio-temporal plots of the plasma emission at 706.5 nm (first row) and simulation results for the electron impact excitation rate from the He I ground state into the He I $(3s)^3S_1$-state (second row) for different flow rates of N_2 of 0.5, 2.5, and 5 sccm (columns) at a constant flow rate of 1 slm of He and at a constant driving

voltage amplitude of 315 V. Further panels of figure 6 depict the computed EEPFs within the same ROIs as before and on space and time average (third row), as well as the computed time averaged spatial distributions of the helium metastable density (fourth row). In the simulation, the surface coefficients are chosen to be the same as used for the voltage variation discussed above. Again, very good agreement between experimental and computational results is found for all reactive gas flows. At the lowest N_2 flow of 0.5 sccm, the discharge is operated in a hybrid combination of the Penning- and the Ω-modes. Increasing the reactive gas flow induces a transition into a pure Ω-mode, since the collisionality is increased by adding a larger admixture of the molecular nitrogen gas. Therefore, at the time of maximum sheath voltage electrons gain less energy over one mean free path by the acceleration by the sheath electric field and the corresponding emission/excitation maximum at the time of maximum sheath voltage decreases as a function of the N_2 gas flow.

Similarly to the behavior of the EEPFs uncovered in figure 5 as a function of the driving voltage amplitude, we also observe significant spatial and temporal variations of this function with the nitrogen flow rate in figures 6(g)–(i). The 'Penning'-EEPF is depleted at high energies as the N_2 flow rate is increased due to the enhanced collisionality and energy losses of electrons, i.e. electrons hardly gain enough energy to excite and to generate helium metastables inside the sheaths. The 'Ω'-EEPF is also influenced by the nitrogen content in a similar way, although to a smaller extent. The spatio-temporally averaged EEPF is again found to be insensitive on the discharge conditions. The density distribution of the helium metastable atoms (panels (j)–(l)) shows a significant change of shape as a function of the flow rate of nitrogen. This is caused by the fact that highly energetic electrons are generated inside the sheaths at low N_2 admixtures, while this is not the case at high reactive gas admixtures. Thus, two-peaks of the metastable density are generated in the sheath regions at low nitrogen admixture, while a single central peak is observed at high reactive gas flows. Moreover, the peak value of the helium metastable density decreases as a function of N_2 admixture, since fewer metastables are generated due to the depleted high energy tail of the EEPF and the 'consumption' of metastables by Penning ionization is increased due to the presence of more nitrogen molecules. A similar dependence of the helium metastable density on the oxygen admixture was observed in helium-oxygen atmospheric pressure RF plasma jets [87]. Overall, the shape of the EEPF changes as a consequence of the mode transition to the Ω-mode in the same way as discussed for the voltage variation.

3.3. The physical origin of the Penning mode

The presence of striations in figures 5 and 6 indicates a significant contribution of ion induced secondary electrons emitted from the electrodes, that are accelerated towards the bulk by the sheath electric field, to the ionization maxima adjacent to both electrodes at the times of maximum sheath voltage within the RF period. In fact, our simulation results show that there are two phenomena that contribute to this maximum: (i) a direct channel, i.e. emission/excitation caused by electrons generated directly by Penning ionization inside the sheaths and (ii) an indirect channel, i.e. secondary electrons emitted from the electrodes due to the impact of positive ions generated by Penning ionization. In order to illustrate this finding and to quantify the respective contributions of each channel, the surface coefficients are changed systematically in the simulations at otherwise fixed discharge conditions and the consequences of this parameter variation on the spatio-temporal excitation dynamics is studied. The discharge conditions are chosen in a way that ensures operation of the plasma in the Penning mode. This requires a high driving voltage amplitude of 355 V and a low N_2 flow of 0.5 sccm. Under these conditions N_2^+ is the dominant ionic species and ion induced SEE is mostly caused by N_2^+ ion impact at the electrodes. In order to switch ion induced SEE on and off either $\gamma_{N_2^+} = 0.1$, $\gamma_{He^+} = 0.3$, $\gamma_{He_2^+} = 0.2$ are used as input parameters for the simulations (SEE on) or $\gamma_{N_2^+} = \gamma_{He^+} = \gamma_{He_2^+} = 0$ are used (SEE off). Moreover, the electron reflection from the electrodes is also switched on and off by changing α between 0 and 0.5. Figure 7 shows the measured spatio-temporal plasma emission at 706.5 nm (figure 7(a)) as well as simulation results of the spatio-temporal electron impact excitation rate from the He ground state into the upper level of the experimentally observed emission line for different choices of the surfaces coefficients (see table 2).

Figure 7(a) shows that the plasma is operated in the Penning mode in the experiment, i.e. the emission maxima at the times of maximum sheath voltage are dominant. Figure 7(b) shows that the experimental results are reproduced well by the simulation, if SEE and electron reflection are switched on. If both surface processes are switched off (7(c)), the excitation maxima at the times of maximum sheath voltage are strongly reduced, i.e. the discharge is predominantly operated in the Ω-mode in the simulation and the experimental result is not reproduced. Under these conditions the remainder of the excitation at the times of maximum sheath voltage is caused by the direct channel of Penning ionization. This result shows that the indirect channel, i.e. contributions of ion induced secondary electrons to this excitation maximum, plays an important role and must not be neglected. Switching SEE on, while keeping electron reflection switched off (see figure 7(d)) results in a significant increase of the excitation maxima at the time of maximum sheath voltage relative to the maxima that occur during the sheath expansion phases. However, the ratio between the Penning and the sheath expansion excitation maxima is still lower in the simulation compared to the experiment. This finding indicates that ion induced SEE is important, but that electron reflection enhances this maximum (see figure 7(b)). Switching SEE off again, but activating electron reflection (see figure 7(e)) cannot reproduce the experimental results either. Thus, we conclude that ion induced SEE contributes significantly to the Penning excitation maxima. At atmospheric pressure the mean free path of these electrons is short

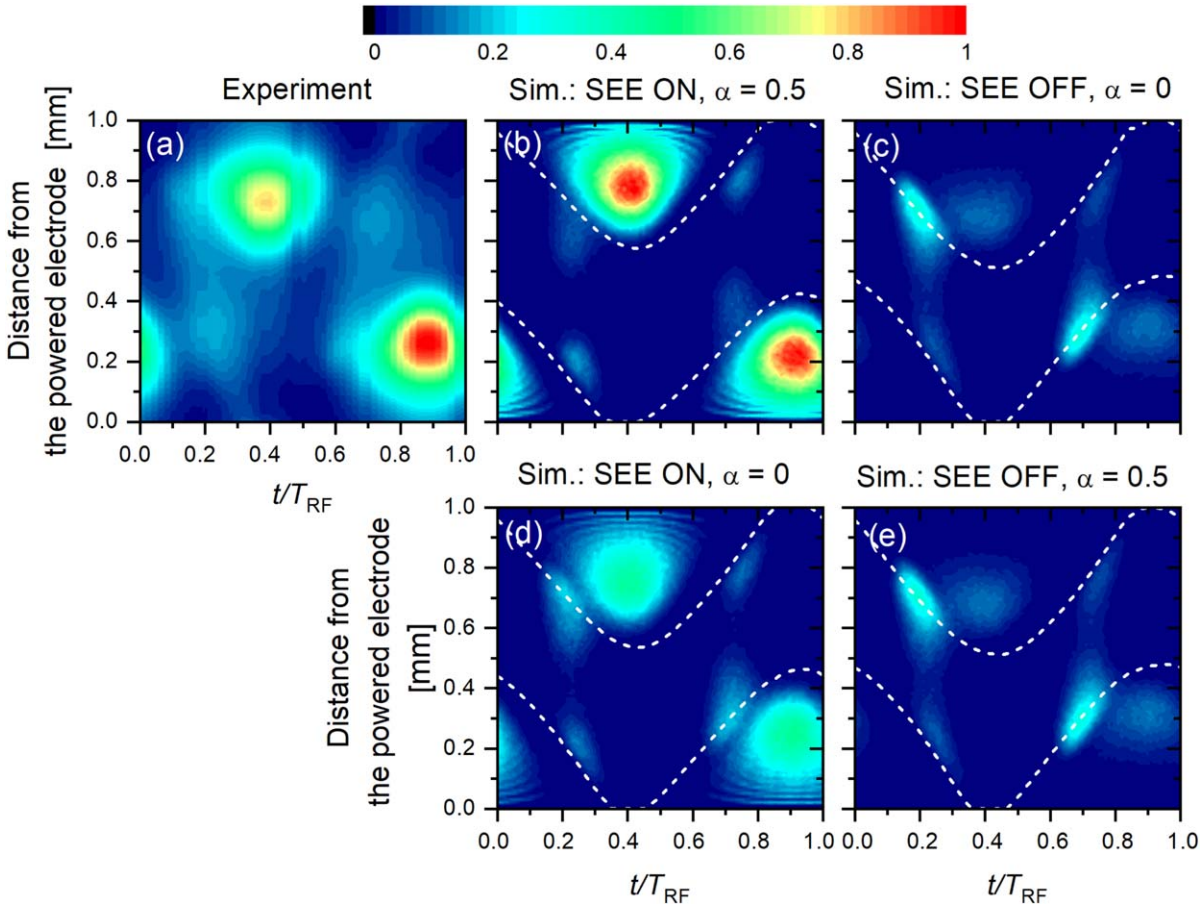

Figure 7. Normalized spatio-temporal plots of the measured emission of the 706.5 nm He I line (a) and normalized (to the maximum value of (b)) spatio-temporal plots of the electron impact excitation rate obtained from the simulations for different choices of the surfaces coefficients listed in table 2. Discharge conditions: 355 V driving voltage amplitude, 1 slm He flow, 0.5 sccm N_2 flow. The powered electrode is situated at $x = 0$, while the grounded electrode is located at $x = 1$ mm. The sheath edge position (white dashed lines) is calculated using the Brinkmann criterion [89] and is shown as white dashed line in the simulation plots.

Table 2. Surface coefficients used in the simulations to obtain spatio-temporal plots of the electron impact excitation rate shown in figure 7.

	$\alpha = 0.5$	$\alpha = 0$
SEE on ($\gamma_{N_2^+} = 0.1$, $\gamma_{He^+} = 0.3$, $\gamma_{He_2^+} = 0.2$)	figure 7(b)	figure 7(d)
SEE off ($\gamma_{N_2^+} = \gamma_{He^+} = \gamma_{He_2^+} = 0$)	figure 7(e)	figure 7(c)

and the reduced electric field at the electrode surfaces is relatively low. Therefore, many of them are reflected back towards the electrode by elastic collisions with neutral atoms/molecules immediately after being emitted from the electrodes [88]. These reflected electrons can reach the electrode again. If electron reflection is neglected in the simulations, these electrons will be absorbed at the electrode. If electron reflection is included, some of them will be reflected back into the plasma and will enhance the Penning ionization maximum. Our results show that this process is important in μ-APPJs under the conditions studied here. Only if ion induced SEE and electron reflection from the electrodes are both included, the PROES measurements can be reproduced and the dynamics of energetic electrons is described correctly by the simulation.

4. Conclusions

The spatio-temporal dynamics of electrons in RF driven micro atmospheric pressure plasma jets (μ-APPJs) operated in different mixtures of He and N_2 was investigated by experimental PROES and computational PIC/MCC simulations. Very good agreement between measurements and computational results was found under all conditions studied here. At a driving frequency of 13.56 MHz two different modes of electron power absorption were observed, i.e. the Ω- and the Penning-mode, depending on the driving voltage amplitude and the concentration of the reactive gas admixture. These modes were identified by characteristic excitation/emission maxima at distinct positions and times within the RF period.

In the experiment, PROES measurements were performed using either no optical filter (wavelength integrated) or in combination with optical filters to monitor the plasma emission from selected lines/bands, i.e. emission of N_2^+, N_2,

and He at 391 nm, around 650 nm, and at 706.5 nm, respectively. Under identical discharge conditions significantly different spatio-temporal plots of the plasma emission were obtained at the different wavelengths. This is explained based on an analysis of the population pathways of the respective excited states and the fact that electron impact excitation from the ground state into these excited states is sensitive to different energy regions of the EEDF. In order to probe the ionization dynamics to understand the plasma generation, a transition should be chosen whose upper level is predominantly excited by electron impact from the ground state and has a high energy threshold. In μ-APPJs, this was found to be the case for the He line at 706.5 nm. This line was previously shown to be useful for visualizing the sheath edge in the discharge [90]. However, our data indicate that at high densities of nitrogen (e.g. figures 6(c) and (f)) an accurate identification of the sheath edges is not possible with this approach. All other lines/bands used in this work were found not to probe the ionization dynamics. Wavelength integrated PROES measurements correspond to a complicated, often unknown superposition of different lines/bands and cannot be used for this purpose either. Generally, our results show that great care must be taken, when choosing an emission line/band for PROES in these systems, since otherwise incorrect conclusions could be drawn and the mode of discharge operation might not be understood correctly.

Increasing the driving voltage amplitude at constant reactive gas flow was found to induce a transition from the Ω- to the Penning-mode due to a stronger acceleration of electrons generated inside the sheaths towards the plasma bulk at higher voltages. Increasing the reactive gas flow at constant voltage was found to induce a transition from the Penning- to the Ω-mode, since the collisionality is increased and electrons cannot gain enough energy to form avalanches inside the sheaths.

By switching ion induced SEE as well as electron reflection at the electrodes on and off in the simulations, the physical origin of the Penning mode was clarified. The characteristic emission/excitation maxima adjacent to the instantaneous sheath edge at the times of maximum sheath voltage within each RF period are not only caused by electrons directly generated by Penning ionization inside the sheaths. Our results show that an indirect channel exists as well, where ion induced secondary electrons emitted from the electrodes contribute to these maxima after being accelerated by the sheath electric field and after being collisionally multiplied. Striations of the excitation rate inside the sheaths were observed and found to be induced by secondary electrons accelerated towards the bulk similar to the Franck–Hertz experiment. Finally, electron reflection from the electrode was found to play an important role as well. At atmospheric pressure, due to the relatively low reduced electric field at the electrodes, many ion induced secondary electrons are reflected back to the electrode, where they were generated, due to elastic electron-neutral collisions. The simulation was found to yield the correct intensity of the Penning excitation maximum observed experimentally only if reflection of these electrons at the electrodes is taken into account, since then electrons are confined, accelerated towards the bulk, and cause additional excitation.

Acknowledgments

This work is supported by the DFG via SFB 1316 (projects A4 and B2), by the Hungarian Office for Research, Development, and Innovation NKFIH grants 119357 and 115805, by US NSF grant PHY 1601080, as well as UK EPSRC grant EP/K018388/1. We would like to thank Nikita Bibinov for useful discussions regarding the population dynamics of N_2-states.

ORCID iDs

I Korolov https://orcid.org/0000-0003-2384-1243
Z Donkó https://orcid.org/0000-0003-1369-6150
J Held https://orcid.org/0000-0003-1206-7504
V Schulz-von der Gathen https://orcid.org/0000-0002-7182-3253
Y Liu https://orcid.org/0000-0002-2680-1338
T Mussenbrock https://orcid.org/0000-0001-6445-4990
J Schulze https://orcid.org/0000-0001-7929-5734

References

[1] Laroussi M 2005 *Plasma Process. Polym.* **2** 391
[2] Becker K H, Schoenbach K H and Eden J G 2006 *J. Phys. D: Appl. Phys.* **39** R55
[3] Kong M G, Kroesen G M W, Morfill G E, Nosenko T, Shimizu T, van Dijk J and Zimmermann J L 2009 *New J. Phys.* **11** 115012
[4] Graves D B 2014 *Phys. Plasmas* **21** 080901
[5] Kim S J, Chung T H, Bae S H and Leem S H 2009 *Plasma Process. Polym.* **6** 676–85
[6] Babayan S E, Jeong J Y, Tu V J, Park J, Selwyn G S and Hicks R F 1998 *Plasma Sources Sci. Technol.* **7** 286
[7] Reuter S, Sousa J S, Stancu G D and van Helden J H 2015 *Plasma Sources Sci. Technol.* **24** 054001
[8] Ichiki T, Tauro R and Horiike Y 2004 *J. Appl. Phys.* **95** 35
[9] Graves D B 2012 *J. Phys. D: Appl. Phys.* **45** 263001
[10] Urashima K and Chang J 2000 *IEEE. Trans. Dielectr. Electr. Insul.* **7** 602–14
[11] Iza F, Lee J K and Kong M G 2007 *Phys. Rev. Lett.* **99** 075004
[12] Eremin D, Hemke T and Mussenbrock T 2016 *Plasma Sources Sci. Technol.* **25** 015009
[13] Birdsall C K and Langdon A B 1985 *Plasma Physics via Computer Simulation* (New York: McGraw-Hill)
[14] Hockney R W and Eastwood J W 1981 *Computer Simulation Using Particles* (New York: McGraw-Hill)
[15] Birdsall C K 1991 *IEEE Trans. Plasma Sci.* **19** 65
[16] Verboncoeur J P 2005 *Plasma Phys. Control. Fusion* **47** A231
[17] Donkó Z 2011 *Plasma Sources Sci. Technol.* **20** 024001
[18] Niermann B, Hemke T, Babaeva N Y, Böke M, Kushner M J, Mussenbrock T and Winter J 2011 *J. Phys. D: Appl. Phys.* **44** 485204

[19] Hemke T, Wollny A, Gebhardt M, Brinkmann R P and Mussenbrock T 2011 *J. Phys. D: Appl. Phys.* **44** 285206
[20] Kushner M J 2005 *J. Phys. D: Appl. Phys.* **38** 1633
[21] Liu D W, Iza F and Kong M G 2009 *Appl. Phys. Lett.* **93** 261503
[22] de Rosny G, Mosburg E R, Abelson J R, Devaud G and Kerns R C 1983 *J. Appl. Phys.* **54** 2272
[23] Schulz-von der Gathen V, Schaper L, Knake N, Reuter S, Niemi K, Gans T and Winter J 2008 *J. Phys. D: Appl. Phys.* **41** 194004
[24] Gans T, Schulz-von der Gathen V and Döbele H F 2004 *Contrib. Plasma Phys.* **44** 523–8
[25] Schulze J, Schüngel E, Donkó Z, Luggenhölscher D and Czarnetzki U 2010 *J. Phys. D: Appl. Phys.* **43** 124016
[26] Benedikt J, Hofmann S, Knake N, Bottner H, Reuter R, von Keudell A and Schulz-von der Gathen V 2010 *Eur. Phys. J.* D **60** 539–46
[27] Reuter S, Winter J, Iseni S, Peters S, Schmidt-Bleker A, Dünnbier M, Schäfer J, Foest R and Weltmann K D 2012 *Plasma Sources Sci. Technol.* **21** 034015
[28] Schaper L, Waskoenig J, Kong M G, Schulz-von der Gathen V and Gans T 2011 *IEEE Trans. Plasma Sci.* **39** 2370
[29] Dünnbier M, Becker M M, Iseni S, Bansemer R, Loffhagen D, Reuter S and Weltmann K D 2015 *Plasma Sources Sci. Technol.* **24** 065018
[30] Greb A, Niemi K, O'Connell D and Gans T 2014 *Appl. Phys. Lett.* **105** 234105
[31] Waskoenig J, Niemi K, Knake N, Graham L M, Reuter S, Schulz-von der Gathen V and Gans T 2010 *Plasma Sources Sci. Technol.* **19** 045018
[32] Gans T, Lin C C, Schulz-von der Gathen V and Döbele H F 2003 *Phys. Rev.* A **67** 012707
[33] Bibinov N K, Bratsev V F, Kokh D B, Ochkur V I and Wiesemann K 2005 *Plasma Sources Sci. Technol.* **14** 109
[34] Fantz U, Briefi S, Rauner D and Wünderlich D 2016 *Plasma Sources Sci. Technol.* **25** 045006
[35] Bibinov N, Halfmann H and Awakowicz P 2008 *Plasma Sources Sci. Technol.* **17** 035004
[36] Offerhaus B, Lackmann J W, Kogelheide F, Bracht V, Smith R, Bibinov N, Stapelmann K and Awakowicz P 2017 *Plasma Process. Polym.* **14** 1600255
[37] Fiebrandt M, Hillebrand B, Spiekermeier S, Bibinov N, Böke M and Awakowicz P 2017 *J. Phys. D: Appl. Phys.* **50** 355202
[38] Hemke T, Eremin D, Mussenbrock T, Derzsi A, Donkó Z, Dittmann K, Meichsner J and Schulze J 2013 *Plasma Sources Sci. Technol.* **22** 015012
[39] Golda J *et al* 2016 *J. Phys. D: Appl. Phys.* **49** 084003
[40] Kawamura E, Lieberman M A, Lichtenberg A J, Chabert P and Lazzaroni C 2014 *Plasma Sources Sci. Technol.* **23** 035014
[41] Maletić D, Puač N, Lazović S, Malović G, Gans T, Schulz-von der Gathen V and Petrović Z L 2012 *Plasma Phys. Control. Fusion* **54** 124046
[42] Schulze J, Heil B G, Luggenhölscher D, Brinkmann R P and Czarnetzki U 2008 *J. Phys. D: Appl. Phys.* **41** 195212
[43] Schulze J, Heil B G, Luggenhölscher D and Czarnetzki U 2008 *IEEE Trans. Plasma Sci.* **36** 1400
[44] Wilczek S, Trieschmann J, Schulze J, Schüngel E, Brinkmann R P, Derzsi A, Korolov I, Donkó Z and Mussenbrock T 2015 *Plasma Sources Sci. Technol.* **24** 024002
[45] Schulze J, Donkó Z, Heil B G, Luggenhölscher D, Mussenbrock T, Brinkmann R P and Czarnetzki U 2008 *J. Phys. D: Appl. Phys.* **41** 105214
[46] Horváth B, Daksha M, Korolov I, Derzsi A and Schulze J 2017 *Plasma Sources Sci. Technol.* **26** 124001
[47] Schröder D, Burhenn S, de los Arcos T and Schulz-von der Gathen V 2015 *J. Phys. D: Appl. Phys.* **48** 055206
[48] Belenguer P and Boeuf J P 1990 *Phys. Rev.* A **41** 4447
[49] Schulze J, Derzsi A, Dittmann K, Hemke T, Meichsner J and Donkó Z 2011 *Phys. Rev. Lett.* **107** 275001
[50] Birdsall C K 1991 *IEEE Trans. Plasma Sci.* **19** 65
[51] Verboncoeur J P 2005 *Plasma Phys. Control. Fusion* **47** A231
[52] Matyash K, Schneider R, Taccogna F, Hatayama A, Longo S, Capitelli M, Tskhakaya D and Bronold F X 2007 *Contrib. Plasma Phys.* **47** 595
[53] Cross sections extracted from program MAGBOLTZ, version 7.1 June 2004, http://lxcat.laplace.univ-tlse.fr
[54] Gordillo-Vazquez F J and Donkó Z 2009 *Plasma Sources Sci. Technol.* **18** 34021
[55] SIGLO database, http://lxcat.net/SIGLO (Retrieved: 10 August 2018)
[56] Nagy O 2002 *Chem. Phys.* **286** 106
[57] Itikawa Y 2006 *J. Phys. Chem. Ref. Data* **35** 31–53
[58] The cross section is extracted from MAGBOLTZ, Biagi S F, version 8.9, http://lxcat.net/Biagi, August 2018
[59] Donkó Z, Hamaguchi S and Gans T 2018 *Plasma Sources Sci. Technol.* **27** 054001
[60] Phelps A V 1994 *J. Appl. Phys.* **76** 747
[61] Brok W J M, Bowden M D, van Dijk J, van der Mullen J J A M and Kroesen G M W 2005 *J. Appl. Phys.* **98** 13302
[62] Sakiyama Y and Graves D B 2006 *J. Phys. D: Appl. Phys.* **39** 3644
[63] Bronshtein I M and Fraiman B S 1969 *Secondary Electron Emission* (Moscow: Atomizdat)
[64] Zalm P C and Beckers L J 1984 *Philips J. Res.* **39** 61–76
[65] Szapiro B, Rocca J J and Prabhuram T 1988 *Appl. Phys. Lett.* **53** 358
[66] Ferrón J, Alonso E V, Baragiola R A and Oliva-Florio A 1981 *J. Phys. D: Appl. Phys.* **14** 1707
[67] Phelps A V 1960 *Phys. Rev.* **117** 619
[68] Pothiraja R, Ruhrmann C, Engelhardt M, Bibinov N and Awakowicz P 2013 *J. Phys. D: Appl. Phys.* **46** 464012
[69] Lofthus A and Krupenie P H 1977 *J. Phys. Chem. Ref. Data* **6** 113
[70] Yang N X, Dong C Z and Jiang J 2012 *J. At. Mol. Sci.* **3** 49–58
[71] Alves L L 2014 *J. Phys.: Conf. Ser.* **565** 012007
[72] Niemi K, Schulz-von der Gathen V and Döbele H F 2005 *Plasma Sources Sci. Technol.* **14** 375
[73] Donkó Z, Schulze J, Hartmann P, Korolov I, Czarnetzki U and Schüngel E 2010 *Appl. Phys. Lett.* **97** 081501
[74] Schulze J, Donkó Z, Schüngel E and Czarnetzki U 2011 *Plasma Sources Sci. Technol.* **20** 045007
[75] Liu Q, Liu Y, Samir T and Ma Z 2014 *Phys. Plasmas* **21** 083511
[76] Robson R E, White R D and Petrović Z L 2005 *Rev. Mod. Phys.* **77** 1303
[77] Pitchford L C, Boeuf J P, Segur P and Marode E 1990 *Nonequilibrium Effects in Ion and Electron Transport* ed J W Gallagher (New York: Plenum Press) (https://doi.org/10.1007/978-1-4613-0661-0)
[78] Kudryavtsev A A, Morin A V and Tsendin L D 2008 *Tech. Phys.* **53** 1029
[79] Korolov I, Vass M, Bastykova N K and Donkó Z 2016 *Rev. Sci. Instrum.* **87** 063102
[80] Magyar P, Korolov I and Donkó Z 2012 *Phys. Rev.* E **85** 056409
[81] Dujko S, White R D and Petrović Z L 2008 *J. Phys. D: Appl. Phys.* **41** 245205
[82] Sigeneger F, Winkler R and Robson R E 2003 *Contrib. Plasma Phys.* **43** 178
[83] Loffhagen D, Winkler L R and Donko Z 2002 *Eur. Phys. J. Appl. Phys.* **18** 189

[84] Kolobov I and Arslanbekov R R 2006 *IEEE Trans. Plasma Sci.* **34** 895
[85] White D, Robson R E, Dujko S, Nicoletopoulos P and Li B 2009 *J. Phys. D: Appl. Phys.* **42** 194001
[86] Niermann B, Kanitz A, Böke M and Winter M 2011 *J. Phys. D: Appl. Phys.* **44** 325201
[87] Niemi K, Waskoenig J, Sadegi N, Gans T and O'Connell D 2011 *Plasma Sources Sci. Technol.* **20** 055005
[88] Phelps A V and Lj Petrović Z 1999 *Plasma Sources Sci. Technol.* **8** R21–44
[89] Brinkmann R P 2007 *J. Appl. Phys.* **102** 093303
[90] Liu D W, Iza F and Kong M G 2009 *Appl. Phys. Lett.* **95** 031501